Elsevier Editorial System(tm) for Molecular Catalysis

Manuscript Draft

Manuscript Number:

Title: Bimetallic Ni-Co/SBA-15 Catalysts for Reforming of Ethanol: How Cobalt Modifies the Nickel Metal Phase and Product Distribution

Article Type: Research Paper

Section/Category: Heterogeneous catalysis

Keywords: nickel cobalt catalysts; in situ XPS; hydrogen production; cobalt carbide; ethanol steam reforming

Corresponding Author: Professor Alfonso Caballero,

Corresponding Author's Institution: University of Seville

First Author: Alfonso Caballero

Order of Authors: Alfonso Caballero; Alberto Rodriguez-Gomez

Abstract: In this study, five mono and bimetallic xNi-(10-x)Co/SBA-15 catalysts (x=10, 8, 5, 2 and 0, with a total metallic content of 10 wt%) have been synthesized using a deposition-precipitation (DP) methodology. Catalytic performances on the steam reforming of ethanol reaction (SRE) have been determined and correlated with their physical and chemical state. A nickel content of 5% or higher yields catalytic systems with good activity, high selectivity to hydrogen and a low production of acetaldehyde (less than 5%). However, in the systems where the cobalt is the main component of the metallic phase (8-10 %), the selectivity changes, mainly due to the production of an excess of acetaldehyde, which is also reflected in the larger H2/CO2 ratio. In agreement with previous findings, this important modification in the selectivity comes from the formation of a cobalt carbide phase, where only takes place in the cobalt enriched systems, and is inhibited with nickel content larger than 5%. The formation of this carbide phase seems to be responsible for the decrease of cobalt particle size during the SRE reaction. Even though this cobalt carbide phase is thermodynamically metastable against decomposition to metallic cobalt and graphite carbon, our results have shown that it only reacts and decomposes after a hydrogen treatment at 600 oC.

***Graphical Abstract**

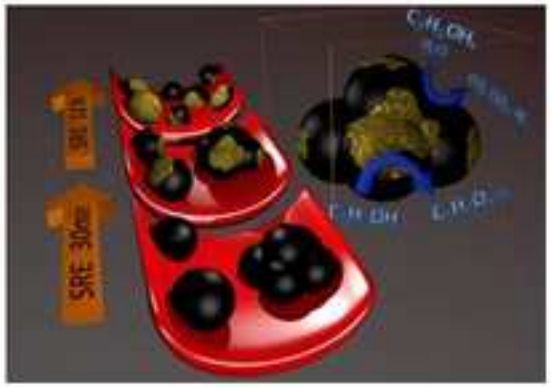

Highlights

- **Five Ni and/or Cobalt catalysts supported on SBA-15 has been prepared by reduction of highly dispersed nickel/cobalt silicate phases**
- **Both metals form a bimetallic phase and the presence of nickel improves the dispersion of cobalt metallic phase**
- **When Co is the main metallic component, a carbide phase is formed during the ethanol reforming reaction**
- **This carbide phase increases the acetaldehyde production and redisperses the cobalt particles**

Bimetallic Ni-Co/SBA-15 Catalysts for Reforming of Ethanol: How Cobalt Modifies the Nickel Metal Phase and Product Distribution

Alberto Rodriguez-Gomez and Alfonso Caballero*
Instituto de Ciencia de Materiales de Sevilla (CSIC-University of Seville) and Departamento de Quimica Inorganica, University of Seville. Av. Americo Vespucio, 49. 41092. Seville, Spain.
caballero@us.es

Abstract

In this study, five mono and bimetallic xNi-(10-x)Co/SBA-15 catalysts (x=10, 8, 5, 2 and 0, with a total metallic content of 10 wt%) have been synthesized using a deposition-precipitation (DP) methodology. Catalytic performances on the steam reforming of ethanol reaction (SRE) have been determined and correlated with their physical and chemical state. A nickel content of 5% or higher yields catalytic systems with good activity, high selectivity to hydrogen and a low production of acetaldehyde (less than 5%). However, in the systems where the cobalt is the main component of the metallic phase (8-10 %), the selectivity changes, mainly due to the production of an excess of acetaldehyde, which is also reflected in the larger H_2/CO_2 ratio. In agreement with previous findings, this important modification in the selectivity comes from the formation of a cobalt carbide phase, where only takes place in the cobalt enriched systems, and is inhibited with nickel content larger than 5%. The formation of this carbide phase seems to be responsible for the decrease of cobalt particle size during the SRE reaction. Even though this cobalt carbide phase is thermodynamically metastable against decomposition to metallic cobalt and graphite carbon, our results have shown that it only reacts and decomposes after a hydrogen treatment at 600 ^{o}C.

Keywords: nickel cobalt catalysts, *in situ* XPS, hydrogen production, cobalt carbide, ethanol steam reforming, acetaldehyde.

1. Introduction

Although methane steam reforming is currently the most industrial competitive process for obtaining hydrogen [1-3], the impact on climate of using fossil fuels, and the limited availability of methane due to the remote locations of some of the major

natural gas fields makes the use of renewable chemicals as bioethanol a very interesting alternative to reduce the environmental impact [4,5]. This product of the biomass processing is easily available, with low toxicity and also very important, the existing infrastructure for storage and transportation is spread worldwide [6-8]. Ethanol steam reforming has been extensively studied in the last decades. As in other reactions such as the methane reforming, the use of noble metals yields good catalytic performance with high selectivity to hydrogen and a limited amount of carbon deposits poisoning the catalyst [9-14]. Once again, the high price and poor availability of metals as Ru, Pt, Rh or Pd, advises the use of cheaper alternatives, especially Ni, but also Co and/or Cu [15-19], even though these metals favor the deposition of carbonaceous deposits. The carbon deposition processes can be mitigated in several ways, as changing the ethanol/water ratio, introducing oxygen in the feed mixture or using different kind of supports [20,21]. An alternative strategy to overcome this issue involves the use of bimetallic systems, where the synergistic effects of the two metals can improve their catalytic performances. In this sense Ni-Co is one of the most popular couple being used for this SRE reaction but also for reforming of methane [19,22-26]. It has been previously reported that the combining effect of this two metals is able to produce less amount but also less harmful carbon deposits [6].

In this work we have synthesized five catalysts containing nickel and/or cobalt supported on the mesoporous silica SBA-15. The catalytic systems, with a total metal loading of 10 wt%, has been prepared by means of a deposition-precipitation method (xNi-(10-x)Co/SBA-15 catalysts, x=10, 8, 5, 2 and 0). We have measured the catalytic performances of these systems, and characterized their states after calcination, hydrogen reduction and steam reforming of ethanol reaction conditions using among others, XPS, XAS and TEM. The results have allowed correlating the catalytic performances with the initial state of metallic phases and its evolution under catalytic conditions. The formation of a Ni-Co bimetallic phase and the stabilization of a cobalt carbide phase in the Co-enriched systems are the major factors determining the catalytic performances of these Ni-Co/SBA-15 catalysts.

2. Experimental

2.1. Preparation of the catalysts

Ni-Co catalytic systems were synthesized by a deposition-precipitation method over a mesoporous support of SBA-15 which was prepared by the Zhao et al. protocol [27] using a TEOS/P123/HCl/H_2O (TEOS: Sigma-Aldrich, CAS: 78-10-4; HCl: Sigma-Aldrich, CAS: 7647-01-0; Pluronic® P-123: Sigma-Aldrich, CAS: 9003-11-6) molar relation of 1/0.02/9.91/320. Typically, 3 g of PEG-PPG-PEG (P123) were dissolved in 140 mL of HCl 1.8 M. After total solution, the mix was heated up to 50 ^{o}C and 5.9 mL of TEOS were added with stirring. The solution was kept on static at 50 ^{o}C for 18 hours, and the gel obtained was filtered and washed several times with distilled water. The product was dried and calcined on static air for 3 hours at 550 ^{o}C. The metallic phase was loaded by heating up to 105 ^{o}C during 2 hours a solution containing 1 g of as-prepared SBA-15, 150 mL of HNO_3 0.01 M (Sigma-Aldrich, CAS: 7697-37-2), the metal precursors [$Ni(NO_3)_2{\cdot}6H_2O$ (Panreac, CAS: 13478-00-7) or/and $Co(NO_3)_2{\cdot}6H_2O$ (Panreac, CAS: 10026-22-9] and 11.37 g of urea (Alfa Aesar, CAS: 57-13-6), for a total metallic charge of 10% and different xNi/(10-x)Co ratio (x=0, 2, 5, 8, 10). After this time, the resulting solution was filtered and washed with distilled water, dried at 110 ^{o}C and calcined on static air for 3 hours at 550 ^{o}C.

2.2. Catalytic test

SRE catalytic tests were performed over 100 mg of catalyst held in a tubular quartz reactor. Samples were pre-reduced in hydrogen at 750 ^{o}C for 1 hour using a heating ramp of 10 ^{o}C·min-1 and reaction was carried out at 500 ^{o}C by injecting 0.02 mL·min-1 of a H_2O/EtOH solution (3.7 molar ratio) and 100 mL·min^{-1} of helium as carrier gas. Products were analyzed by gas chromatography using an Agilent´s 490 microGC equipment, connected on-line with the reactor, provided with three columns and TCD detectors: two molecular sieves for the analysis of lighter molecules as H_2, CO, CH_4 and CO, and a capillary column (PoraPLOT-U) for the analysis of CO_2, H_2O, ethanol and acetaldehyde. Quantitative calculations were as follows:

Ethanol conversion (%):

$$X_{EtOH} = \frac{F_{EtOH\,in} - F_{EtOH\,out}}{F_{EtOH\,in}} \cdot 100\,,$$

being F_{EtOHin} and $F_{EtOHout}$ the ethanol molar flow in the inlet and outlet gas, respectively.

Selectivity to different products (%):

$$S_i = \frac{F_{i\,out}}{c_i(F_{EtOH\,in} - F_{EtOH\,out})} \cdot 100 \quad ,$$

being F_i the component *i* molar flow. C_i is a stoichiometric value obtained by the equation: $c_i = \frac{\text{carbon atoms in EtOH}}{\text{carbon atoms in } i}$

In the case of H_2 selectivity we estimated the value given by the EtOH/H_2 stoichiometric relation in SRE, being c_i=6.

2.3. N_2-physisorption

N_2 adsorption/desorption isotherms were obtained at -196 ^{o}C in a TRISTAR II (Micromeritics) equipment. With a minimum amount of 50 mg, each sample was pre-treated under vacuum at 150 ^{o}C prior to the adsorption/desorption experiment. Surface areas and porosity were calculated according to the BET and BJH method, respectively.

2.4. TEM

Transmission electron microscopy was carried out in a Philips CM200 microscope operating at 200 kV using a copper grid coated with lacey carbon as sample support. Analysis of particle size was performed by sampling 150 particles.

2.5. XRD

Diffractogram patterns of calcined and reduced samples were obtained in a PANalytical X-Pert PRO diffractometer with a Cu anode (λ=1.5418 Å, Cu Kα), using a Bragg-Brentano configuration in the 2θ range of 10-80°, with a step of 0.05° and an effective acquisition time of 240 s.

2.6. TPR

Temperature-programmed reduction experiments were done using a thermal conductivity detector calibrated with a commercial NiO. An estimated amount of calcined sample for consuming 100 μmol of H_2 was used in each case. Conventional experiments were carried out from room temperature up to 1000 ^{o}C with a heating ramp of 10 $^{o}C \cdot min^{-1}$. Experimental conditions were chosen to avoid peak coalescence [28]. A mass spectrometer was used to determine the evolution of gases during the reduction treatments of oxidized and post-reaction samples: CH_4 (m/e^-=15), H_2 (m/e^-=2) and H_2O (m/e^-=18).

2.7. XPS

X-ray photoelectron spectroscopy was performed in a VG-ESCALAB 210 equipment. Acquisition was performed in a chamber equipped with a SPECS Phoibos 100 hemispheric analyzer at 10^{-9} Torr using an anticathode of MgKα (E=1.5418 eV) with 12 kV of potential acceleration and 20 mA of current. Catalytic systems were analyzed as-prepared and after different, consecutive in situ treatments:

1. 5%H_2/Ar at 750 ^{o}C during 1 hour with a heating ramp of 10 $^{o}C \cdot min^{-1}$.

2. SRE conditions at 500 ^{o}C during 1 hour by bubbling an ethanol/water solution with 100 $mL \cdot min^{-1}$ of argon for obtaining a similar flow gas composition as the catalytic test.

3. Hydrogen treatment with 5%H_2/Ar at 400 ^{o}C, during 1 hour.

4. Hydrogen treatment with 5%H_2/Ar at 550 ^{o}C, during 1 hour.

5. Hydrogen treatment with 5%H_2/Ar at 600 ^{o}C, during 1 hour.

2.8. XAS

X-ray absorption spectra were carried out at the BL22 CLAESS beamline at the ALBA synchrotron facility (Spain). Pelletized samples were analyzed in transmission mode in an in situ cell for gas-solid reactions with an amount of sample estimated to maximize the signal/noise ratio. Due to beamtime limitations, only monometallic samples were studied. These catalytic systems were analyzed as-prepared and after different in situ treatments:

1. 5%H_2/Ar at 750 ^{o}C during 1 hour with a heating ramp of 10 $^{o}C \cdot min^{-1}$.

2. SRE conditions at 500 ^{o}C during 1 hour by bubbling an ethanol/water solution with 100 mL·min^{-1} of argon for obtaining a similar flow gas composition as the catalytic test.

Standard nickel and cobalt foils were measured and used for energy calibration. XAS spectra were recorded from 7600 to 9200 eV (including both Ni and Co K-edge energies).

3. Results and discussion

3.1. Characterization of calcined and reduced catalysts

The five catalytic systems were characterized by N_2 adsorption analysis (BET, BJH), XRD, TEM, TPR and XPS. XAS spectra were just collected for the two monometallic systems. As reflected in Table 1, during the alkaline treatment with urea, all samples undergo important changes of BET surface area and mean porous size. From the original value of 738 m^2.g^{-1} of the pristine SBA-15, the BET of the treated solids decrease to 250-280 m^2.g^{-1}. Simultaneously, the average pore size increases from 6.7 to 9-12 nm. Despite this loss of surface area and porosity, the images of the calcined catalysts obtained by TEM (Figure 1) shows that the channeled structure of the SBA-15 support is preserved, with the "fibrous" structures of phyllosilicate phases generated during this treatment being visible [29-31]. The formation of $(NiCo)_3Si_2O_5(OH)_4$ and/or $(NiCo)_3Si_4O_{10}(OH)_2$ phyllosilicate phases [32] can be confirmed in the XRD diagrams of Figure 2 (left) by the wide peaks appearing around 35 and 61^{o} [33], the only phases detected in the calcined samples. As it can be observed in the inset, the bimetallic samples, and in particular the 5Ni-5Co/SBA-15, only show one peak near 61^{o}, indicating the formation of a bimetallic nickel cobalt phyllosilicate phase.

According to the TPR profiles included in Figure 3, the 10Ni/SBA-15 catalyst presents two different reduction processes, characterized by a small shoulder at 475 ^{o}C and a main peak centered at 675 ^{o}C, previously assigned to the reduction of a small amount of nickel oxide and a nickel phyllosilicate phase, respectively [29,34]. Likewise, the 10Co/SBA-15 system has the main peak at higher temperature (750 ^{o}C) with a shoulder centered at 850 ^{o}C [26]. All the bimetallic catalysts present intermediate profiles, with the main peak centered at higher temperatures as the cobalt content

increases. Thus, these profiles once again suggest the formation of bimetallic phases in the calcined catalysts. The diffraction diagrams of these systems reduced in hydrogen at 750 ^{o}C, included in Figure 2 (right) show diffraction peaks around 44.5 and 52^{o}, the result of well reduced nickel and/or cobalt phases. As detailed in the figure, the shift of these peaks with the Ni/Co content also suggests the formation of a Ni-Co bimetallic phase.

The TEM images of the catalytic systems obtained after hydrogen reduction are depicted in Figure 4. It can be observed how the sizes of the metallic particles are dependent on the Ni/Co ratio. Thus, the smaller particles (4-6 nm, black bars in Figure 5) are obtained for the 10Ni/SBA-15 catalyst, and the size progressively increases with the Co content, reaching an average value of 14.4 nm for the 10Co/SBA-15 (Table 1). These results clearly show a stronger interaction of nickel with the SBA-15 support, allowing a larger dispersion of the metallic phase. Additionally, both Figure 4 and 5 show that the increasing amount of cobalt gives rise to higher size heterogeneity, reaching a range around 3-25 nm in the monometallic 10Co/SBA-15 system.

XPS spectroscopy of these five catalysts has shed light on the origin of the observed differences in particle sizes. Figure 6a depicts the contiguous Ni 2p and Co 2p XPS regions of calcined samples, showing the presence of Ni^{2+} and Co^{2+} species of metal phyllosilicates, respectively [35-39]. As the nickel and cobalt contents are different in each system, the spectra are better understood when normalized to the respective Ni and Co contents (Figure 6b). Quantification of peaks intensities are presented in Table 2, where nominal and normalized to the metal content values is included for each catalytic system. Thus, while for calcined samples the normalized intensity of nickel remains virtually unchanged (0.9±0.1), cobalt is strongly affected by the presence of nickel so that it increases the dispersion over the SBA-15 support when the amount of nickel increases. Especially striking is the high intensity of the Co 2p signal obtained for 8Ni-2Co/SBA-15, more than two times the normalized value of the cobalt monometallic system (0.48 and 1.09, respectively). Anyhow, these results indicate that the smaller particle sizes obtained for the reduced nickel containing catalysts are related with the initial better dispersion of the phyllosilicate phases generated by calcination. It can be also seen in Table 2 how after reduction the intensity of Ni 2p peaks included in Figure 7 slightly decreases by the presence of

cobalt (0.25 to 0.17), while the Co 2p region signals increases 3.5 times its normalized intensity when nickel is present, from 0.09 in the Co/SBA-15 to 0.31 in 8Ni-2Co/SBA-15. These results are in agreement with the previous characterization data indicating an important increase in the cobalt dispersion when in the bimetallic systems.

3.2. Steam reforming of ethanol

The catalytic performances of the five Ni-Co/SBA-15 systems were studied in the steam reforming of ethanol reaction (SRE) at 500 ^{o}C using an H_2O:EtOH ratio of 3.7. Table 3 includes conversion and selectivity values after 12 h on stream. After an initial deactivating interval of 1-2 hours, all the catalytic systems were stable without noticeable deactivation during the whole studied period under ethanol reforming conditions. As shown, ethanol conversion values range from 60 to 90%, but other important differences can be noted among the five catalytic systems. Both 10Ni/SBA-15 and 5Ni-5Co/SBA-15 have exactly the same behaviour in conversion and selectivity towards all products, including a H_2/CO_2 ratio near 1. However, the 8Ni-2Co/SBA-15, with an intermediate metallic composition presents a higher conversion up to 85.6%, in part due to the higher production on methane (21% versus 14%). This change is accompanied by the almost total disappearance of the product acetaldehyde, which had reached values close to 4% in the first two described catalysts. As this catalyst presents the higher cobalt dispersion as determined by XPS (Table 2) and a Ni/Co ratio of 4, this singular behaviour could be related with the formation of a homogeneous well dispersed Ni_4Co_1 bimetallic phase. Finally, the 2Ni-8Co/SBA-15 and 10Co/SBA-15 are characterized by the successive increase in the selectivity to acetaldehyde (8.5 and 43.5%, respectively), together with a parallel increase in the H_2/CO_2 ratio (1.12 and 1.42), revealing the gradual high dehydrogenation activity of these two catalytic systems ($C_2H_5OH \rightarrow C_2H_4O + H_2$). It is worth to mention that the high performance of the 10Co/SBA-15 catalyst for acetaldehyde production had been previously reported by our group as a result of the formation of a cobalt carbide phase under SRE reaction conditions [3]. Other authors also reported cobalt containing catalytic systems presenting values for acetaldehyde production with selectivity values up to 50% [40,41].

3.3. Characterization studies after steam reforming of ethanol

In order to clarify the origin of the different catalytic performances in the catalytic systems studied in this work, we have performed additional characterization studies after submitting the catalysts to SRE reaction conditions. Thus, after the SRE reaction the catalysts present the appearance showed in the TEM images of Figure 8. According to the analysis of particles sizes in the five systems (see histograms included in Figure 5), two different behaviors can be observed. The two systems with the higher Ni content essentially maintain their size and distribution of the freshly reduced 10Ni and 8Ni-2Co/SBA-15 catalysts. Surprisingly, the analysis of the TEM images of both catalysts with the higher cobalt content (2Ni-8Co and 10Co/SBA-15) makes it clear that the particle size decreases, which is more evident in the 10Co/SBA-15 catalyst, where no nickel is present. According to our previous findings [3], this unexpected redispersion of metallic particles could be related to the formation of a cobalt carbide phase, which apparently breaks the cobalt metallic particles, significantly reducing the particle size. In turn, this phenomenon seems to correlate with the higher acetaldehyde production observed in these two systems (Table 3). In order to deepen the origin of this phenomenon, we have carried out an *in situ* XPS study of the catalysts after the SRE reaction, which results are depicted in Figure 9. The comparison between the spectra before and after SRE reaction shows essentially that there are no significant changes in the Ni 2p region of the four Ni-containing catalysts, except for a slight increase in the intensity for the 2Ni-8Co/SBA-15, which agrees with higher dispersion after reaction observed previously by TEM (Figure 5). In a first inspection, a similar behavior is observed in the Co 2p region of the two more Ni-enriched systems (8Ni-2Co and 5Ni-5Co/SBA-15), while the Co 2p regions of 2Ni-8Co and especially, 10Co/SBA-15 catalysts are clearly modified, shifting the main peak from 778.0 eV to lower binding energy values. This red shift of cobalt to an apparently more reduced state has been previously observed by us in the monometallic catalytic system and ascribed to the formation of a new cobalt carbide phase under SRE reaction conditions. In fact, the observed peak is an envelope of two different ones coming from a mixture of cobalt carbide (centered at 776.6 eV) and metallic phases (centered at 778.0 eV) [3]. Deconvolution of this peak reveals the presence of 70 % metallic cobalt, 30 % cobalt carbide in the 10Co/SBA-15 catalyst, and 79 % metallic cobalt, 21 %

of cobalt carbide in the 2Ni-8Co/SBA-15 catalyst. The different amounts of carbide phase detected in these catalysts could account for the different acetaldehyde production observed in these two catalytic systems (Table 3). In this sense, it is worth to mention that, although less obvious, even the Co 2p region of 5Ni-5Co/SBA-15 presents a small red shift which can be convoluted with a 10 % contribution of a cobalt carbide phase at 776.6 eV. The fact that this catalyst has the same acetaldehyde production as the 10Ni/SBA-15 indicates that there is a minimum amount of carbide needed to increase the acetaldehyde production. This could be due to the fact that the adsorption of ethanol on the cobalt surface, the first step in both reforming and dehydrogenation of ethanol, is a structure sensitive reaction [20] and therefore needing the formation of a specific ensemble of active atoms to constitute the cobalt carbide active site.

3.4. Further characterization of carbide phase

In order to understand the state of this carbide phase, a new set of TPR experiments have been performed. In this case, a first TPR has been recorded just up to 750 ^{o}C, maintaining isothermally the same reducing conditions during 1h. Afterwards, the systems were submitted to SRE reaction conditions at 500 ^{o}C during 1 h and a second TPR recorded. The two TPR profiles are depicted in Figure 10. As expected, the profiles corresponding to the first TPR up to 750 ^{o}C (thin line) are similar to those of Figure 3. Likewise, all the profiles of the second TPRs (thick line) have two distinct parts. A first positive peak at low temperature (around 520 ^{o}C), indicating depletion of hydrogen, which in the 10Co and 2Ni-8Co/SBA-15 catalysts is accompanied with a shoulder or small peak at 620 ^{o}C. Along with this, a negative peak appears at higher temperature, centred at 750 ^{o}C, which must correspond to desorption of previously adsorbed hydrogen on the metallic particles. It is important to note that other processes or the formation of other products (i.e. methane) could affect the signal from the TCD detector during TPR, which will be discussed below. Thus, the hydrogen consumption process observed at low temperature (525 ºC) could be due to the reduction of metal particles previously oxidized during the SRE reaction. This possibility has been discarded in view of the results obtained by XAS spectroscopy under similar SRE reaction conditions (Figure 11). As shown in XANES and Fourier

Transform curves, after reaction, both nickel and cobalt remain completely reduced. Thus, the depletion of hydrogen only can be due to reduction of carbon deposited during the SRE reaction, which can be confirmed in Figure 12, where are depicted the TCD and mass spectrometer profiles obtained during the second TPR. Methane (m/e^- =15) is formed coinciding with the depletion of hydrogen (m/e^-=2), confirming that carbon is eliminated in this low temperature process.

However, a deeper comparison of the profiles of the five catalysts shows once again two different patterns. On the one hand, in the three catalysts with the high amount of nickel (10Ni, 8Ni-2Co and 5Ni-5Co/SBA-15) the peak maxima for H_2 and CH_4 approximately appear at the same temperature (521, 527 and 529±3 ^oC, respectively), and consist in asymmetric peaks with a soft tail a high temperature. But the profiles for the two Co-enriched catalysts follow a different pattern. In both cases (10Co and 2Ni-8Co/SBA-15) the m/e^-=2 peak coming from H_2 species is complex, with at less two maxima at different temperatures (528 and 625 ^oC for 10Co/SBA-15; 528 and 610 ^oC for 2Ni-8Co/SBA-15). Moreover, maxima for H_2 and CH_4 do not match, with the maxima for methane appearing at a temperature 35 ^oC higher. The fact that in these two systems the higher methane production does not match the higher hydrogen consumption must indicate that the methane formed during the TPR comes from a different carbon phase, more hydrogenated and therefore consuming less hydrogen. As this effect, much more intense in the cobalt monometallic system, correlates with the amount of cobalt carbide phase in these two systems, it could be due to the hydrogenation of this carbide phase, which is thermodynamically unstable [42], and could adsorb a certain amount of hydrogen before decompose ($CoC_x + H_2 \rightarrow Co^0 + CH_4$).

If this were the case, a hydrogen treatment of the catalysts presenting the cobalt carbide phase should reverse the red shift of the Co 2p peak observed by XPS. As shown in Figure 13, this is really what happens when the 10Co/SBA-15 catalyst is treated under SRE conditions and later in hydrogen at increasing temperatures up to 600 ^oC, the higher reachable in our XPS equipment. The SRE treatment causes the red shift of the Co 2p peak, which does not move significantly when treated in hydrogen till 550 ^oC. At higher temperature, a blue shift is observed, indicating that the carbide phase is decomposing and the metallic cobalt restored.

4. Conclusions

We have characterized five Ni-Co/SBA-15 bimetallic systems active in the steam reforming of ethanol reaction at 500 ^{o}C. The presence of nickel favors the dispersion of metallic phases after reduction, while the cobalt tends to generate larger metallic particles. However, these Co-enriched particles significantly reduce their size after SRE reaction, and in parallel, the higher cobalt content increases the acetaldehyde production. Both effects, high acetaldehyde production and breakage of metallic particles can be explained accepting the formation of a cobalt carbide phase, which although thermodynamically metastable, has proved to remain stable under hydrogen at 550 ^{o}C.

Acknowledgments

We thank the "Ministerio de Economia and Competitividad" of Spain (Projects CTQ2014-60524-R and ENE2017-88818-C2-1-R) and the ESRF facility and staff (BM25 SPLINE beamline), and the ALBA facility and staff (BL22 CLAESS beamline) for their experimental support. A.R.G thanks also the Spanish Government for the PhD fellowship (BES-2012-061744).

References

1. Oyama, S. T.; Hacarlioglu, P.; Gu, Y. F.; Lee, D. *Int. J. Hydrogen Energy* **2012**, *37*, 10444-10450.

2. Bhavani, A. G.; Kim, W. Y.; Lee, J. S. *ACS Catal.* **2013**, *3*, 1537-1544.

3. Rodriguez-Gomez, A.; Holgado, J. P.; Caballero, A. *ACS Catal.* 2017, 7, 5243-5247.

4. Huber, G. W.; Iborra, S.; Corma, A. *Chem. Rev.* **2006**, 106, 4044−4098.

5. Tanksale, A.; Beltramini, J. N.; Lu, G.Q. M. *Renewable Sustainable Energy Rev.* **2010**, 14, 166−182.

6. Sharma, Y. C.; Kumar, A.; Prasad, R.; Upadhyay, S. N. *Renewable Sustainable Energy Rev.* **2017**, 74, 89−103.

7. Wu, C.; Dupont, V.; Nahil, M. A. ; Dou, B. ; Chen, H.; Williams, P. T. *Journal of the Energy Institute* **2017**, 90, 276-284.

8. Chen, J.; Sun, J.; Wang, Y. *Ind. Eng. Chem. Res.* **2017**, 56, 4627−4637.

9. Palma, V.; Castaldo, F.; Ciambelli, P.; Iaquaniello, G. *Appl Catal B: Environmental* **2014**, 145, 73–84.

10. Ito, S-i.; Tomishige, K. *Catal Commun.* **2010**, 12, 157–160.

11. Divins, N. J.; Casanovas, A.; Xu, W.; Senanayake, S. D. ; Wiater, D. ; Trovarelli, A. ; Llorca, J. *Catal Today* **2015**, 253, 99–105.

12. Su, S. ; Li, W. ; Bai, Z. ; Xiang, H. *Int. J. Hydrog. Energy* **2008**, 33, 6947–6952.

13. Goula, M. A. ; Kontou, S. K. ; Tsiakaras, P. E. *Appl. Catal B: Environmental* **2004**, 49, 135–144.

14. Hou, T. F.; Yu, B.; Zhang, S. Y.; Xu, T. K.; Wang, D. Z.; Cai, W. J. *Catal. Commun.* **2015**, 58, 137–140.

15. Song, H.; Ozkan, U. S. *J. Phys. Chem. A* **2010**, 114, 3796–3801.

16. El Doukkali, M.; Iriondo, A.; Arias, P. L.; Cambra, J. F.; Gandarias, I.; Barrio, V. L. *Int. J. Hydrog. Energy* **2012**, 37, 8298–8309.

17. Barroso, M. N.; Galetti, A. E.; Abello, M. C. *Appl. Catal. A: General* **2011**, 394, 124–131.

18. Profeti, L. P. R.; Ticianelli, E. A.; Assaf, E. M. *J. Power Sources* **2008**, 175, 482–489.

19. Duan, S.; Senkan, S. Ind. Eng. Chem. Res. 2005, 44, 6381–6386.

20. Parlett, C. M. A.; Aydin, A.; Durndell, L. J.; Frattini, L.; Isaacs, M. A.; Lee, A. F. ; Liu, X.; Olivi, L.; Trofimovaite, R.; Wilson, K.; Wu, C. *Catal. Commun.* **2017**, 91, 76-79.

21. Mattos, L. V.; Jacobs, G.; Davis, B. H.; Noronha, F. B. *Chem. Rev.* 2012, 112, 4094–4123.

22. Gonzalez-Delacruz, V. M.; Pereñiguez, R.; Ternero, F.; Holgado, J. P.; Caballero, A. *J. Phys. Chem. C* **2012**, 116, 2919–2926.

23. Zhang, J.; Wang, H.; Dalai, A. K. *J. Catal.* **2007**, 249, 300–310.

24.Wang, L.; Li, D.; Koike, M.; Watanabe, H.; Xu, Y.; Nakagawa, Y.; Tomishige, K. *Fuel* **2013**, 112, 654–661.

25. Silva, C. R. B.; Conceicao, L.; Ribeiro, N. F. P.; Souza, M. M. V. M. *Catal. Commun.* **2011**, 12, 665–668.

26. Rodriguez-Gomez, A.; Pereñiguez, R.; Caballero, A. *Catal. Today* **2017**, DOI: 10.1016/j.cattod.2017.02.020.

27. Zhao, D. Y.; Feng, J. L.; Huo, Q. S.; Melosh, N.; Fredrickson, G. H.; Chmelka, B. F.; Stucky, G. D. *Science* **1998**, 279, 548-552.

28. Malet, P.; Caballero, A. *Chem. Soc. Faraday Trans.,* **1988**, 84, 2369-2375.

29. Rodriguez-Gomez, A.; Caballero, A. *ChemNanoMat* **2017**, 3, 94-97.

30. Kong, X. ; Zhu, Y. ; Zheng, H. ; Li, X. ; Zhu, Y. ; Li, Y. *ACS Catal.* **2015**, 5, 5914-5920.

31. Zhang, C. ; Yue, H. ; Huang, Z. ; Li, S. ; Wu, G. ; Ma, X. ; Gong, J. *ACS Sustain. Chem. Eng.* **2012**, 1, 161–173.

32. Kim, J. S.; Park, I.; Jeong, E.; Jin, K.; Seong, W. M.; Yoon, G.; Kim, H.; Kim, B.; Nam, K. T.; Kang, K. *Adv. Mater.* **2017**, 29, 1606893.

33. Galvez, M. E.; Albarazi, A.; Da Costa, P. *Appl. Catal. A: General* **2015**, 504, 143–150.

34. Rodriguez-Gomez, A.; Pereñiguez, R.; Caballero, A. *J. Phys.Chem B* **2017**, DOI: 10.1021/acs.jpcb.7b03835.

35. Espinos, J. P.; Gonzalez-Elipe, A. R.; Caballero, A.; Garcia, J.; Munuera, G. *J. Catal.* **1992**, 136, 415−422.

36. Lu, B.; Ju, Y.; Abe, T.; Kawamoto, K. *RSC Adv.* **2015**, 5, 56444−56454.

37. Todorova, S.; Kadinov, G.; Tenchev, K.; Kalvachev, Y.; Kostov-Kytin, V. *J. Mater. Sci.* **2007**, 42, 3315-3320.

38. Kengne, B. F.; Alayat, A. M.; Luo, G.; McDonald, A. G.; Brown, J.; Smotherman, H.; McIlroy, D. N. *Appl. Surf Sci.* **2015**, 359, 508-514.

39. Todorova, S.; Naydenov, A.; Kolev, H.; Holgado, J. P.; Ivanov, G.; Kadinov, G.; Caballero, A. *Appl. Catal. A: General* **2012**, 413, 43–51.

40. Llorca, J.; Ramirez de la Piscina, P.; Dalmon, J.-A.; Homs, N. *Chem. Mater.* **2004**, 16, 3573−3578.

41. Vizcaíno, A. J.; Carrero, A.; Calles, J. A. *Fuel Process. Technol.* **2016**, 146, 99−109.

42. Zhao, Y. H.; Su, H. Y.; Sun, K.; Liu, J.; Li, W. X. *Surf. Sci.* **2012**, 606, 598−604.

Table 1

Characterization data of the Ni-Co/SBA-15 catalytic systems.

	S_{BET} ($m^2 \cdot g^{-1}$)	Average pore size (nm)[a]	$Ni/Co_{surf.}$ by XPS ($\%_{at}$)	Crystallite size (XRD[b]) [Calc/Red]	Average metallic particle size (TEM[c]) [Red/SRE]
SBA-15	738	6.7	-	-	-
SBA-15 treated with urea	249	9.1	-	-	-
10Ni/SBA-15	283	10.3	11.3/0.0	5.4/4.1	4.3/4.2
8Ni-2Co/SBA-15	272	11.1	7.8/2.6	7.6/4.1	4.4/4.0
5Ni-5Co/SBA-15	261	12.0	4.2/3.1	7.0/4.5	5.9/8.6
2Ni-8Co/SBA-15	269	10.3	1.9/7.1	6.5/8.2	8.6/7.0
10Co/SBA-15 DP	280	9.8	0.0/7.1	5.1/13.2	14.4/9.6

[a] Obtained by the BJH method.

[b] Calculated from the Scherrer equation.

[c] Obtained by sampling 150 particles.

Table 2

Atomic percentage of Ni and/or Co as determined from XPS signals

	Calcined catalysts		Reduced catalysts	
	At% Ni (N%)*	**At% Co (N%)***	**At% Ni (N%)***	**At% Co (N%)***
10Ni/SBA-15	10.89 (1.09)	-	2.5 (0.25)	-
8Ni-2Co/SBA-15	7.88 (0.99)	2.18 (1.09)	2.2 (0.28)	0.61 (0.31)
5Ni-5Co/SBA-15	4.17 (0.83)	3.80 (0.76)	0.73 (0.15)	0.75 (0.15)
2Ni-8Co/SBA-15	1.83 (0.91)	7.14 (0.89)	0.33 (0.17)	0.59 (0.07)
10Co/SBA-15	-	4.78 (0.48)	-	0.9 (0.09)

* **N%: atomic percentage normalized to nominal Ni/Co metal content (10-8%)**

Table 3

Catalytic performances in Steam Reforming of Ethanol after 12h of TOS

	Conv.	Selectivities (%)					
	(%)	H_2	CO_2	H_2/CO_2	CO	CH_4	CH_3CHO
10Ni/SBA-15	69.3	59.4	59.5	1.00	19.6	13.8	3.8
8Ni2Co/SBA-15	85.6	62.4	60.3	1.03	18.3	21.0	0.1
5Ni5Co/SBA-15	68.0	62.2	60.9	1.02	19.1	14.0	4.4
2Ni8Co/SBA-15	59.3	70.1	62.6	1.12	14.2	14.9	8.5
Co/SBA-15	88.6	55.1	38.9	1.42	14.1	3.7	43.5

Figure Captions

Figure 1. TEM images for calcined 10Ni/SBA-15 (a), 8Ni-2Co/SBA-15 (b), 5Ni-5Co/SBA-15 (c), 2Ni-8Co/SBA-15 (d) and 10Co/SBA-15 (e) catalysts.

Figure 2. XRD patterns for (left) calcined and (right) treated in 5%H_2/Ar at 750 ^oC nickel-cobalt-based systems.

Figure 3. Temperature-programmed reduction profiles for the calcined Ni-Co/SBA-15 catalytic systems.

Figure 4. TEM images of 10Ni/SBA-15 (a), 8Ni-2Co/SBA-15 (b), 5Ni-5Co/SBA-15 (c), 2Ni-8Co/SBA-15 (d), and 10Co/SBA-15 (e), after hydrogen reduction at 750 °C.

Figure 5. Histograms of particle sizes for 10Ni/SBA-15 (a), 8Ni-2Co/SBA-15 (b), 5Ni-5Co/SBA-15 (c), 2Ni-8Co/SBA-15 (d), and 10Co/SBA-15 (e), after reduction (black bars) and after being submitted to SRE reaction conditions (red bars).

Figure 6. XPS spectra of calcined Ni-Co/SBA-15 systems (a) and same spectra normalized to metal percentage (b).

Figure 7. XPS spectra of reduced Ni-Co/SBA-15 systems normalized to metal percentage.

Figure 8. TEM images for 10Ni/SBA-15 (a), 8Ni-2Co/SBA-15 (b), 5Ni-5Co/SBA-15 (c), 2Ni-8Co/SBA-15 (d), and 10Co/SBA-15 (e), after SRE reaction.

Figure 9. XPS spectra of reduced (thin line) and spent (thick line) Ni-Co/SBA-15 systems normalized to metal percentage.

Figure 10. TPR profiles of Ni-Co/SBA-15 catalysts up to 750 ^oC plus 1h isotherm. Thin line: first TPR. Thick line: second TPR after SRE reaction.

Figure 11. Co (left) and Ni (right) K-edge XANES spectra and Fourier transform functions of the EXAFS oscillations after different treatments.

Figure 12. TCD and Mass Spectrometer signals coming from H_2 (m/e^-=2) and methane (m/e^-=15) for 10Ni/SBA-15 (a), 8Ni-2Co/SBA-15 (b), 5Ni-5Co/SBA-15 (c), 2Ni-8Co/SBA-15 (d), and 10Co/SBA-15 (e).

Figure 13. XPS spectra of reduced, spent and hydrogenated 10Co/SBA-15 system.

Figure

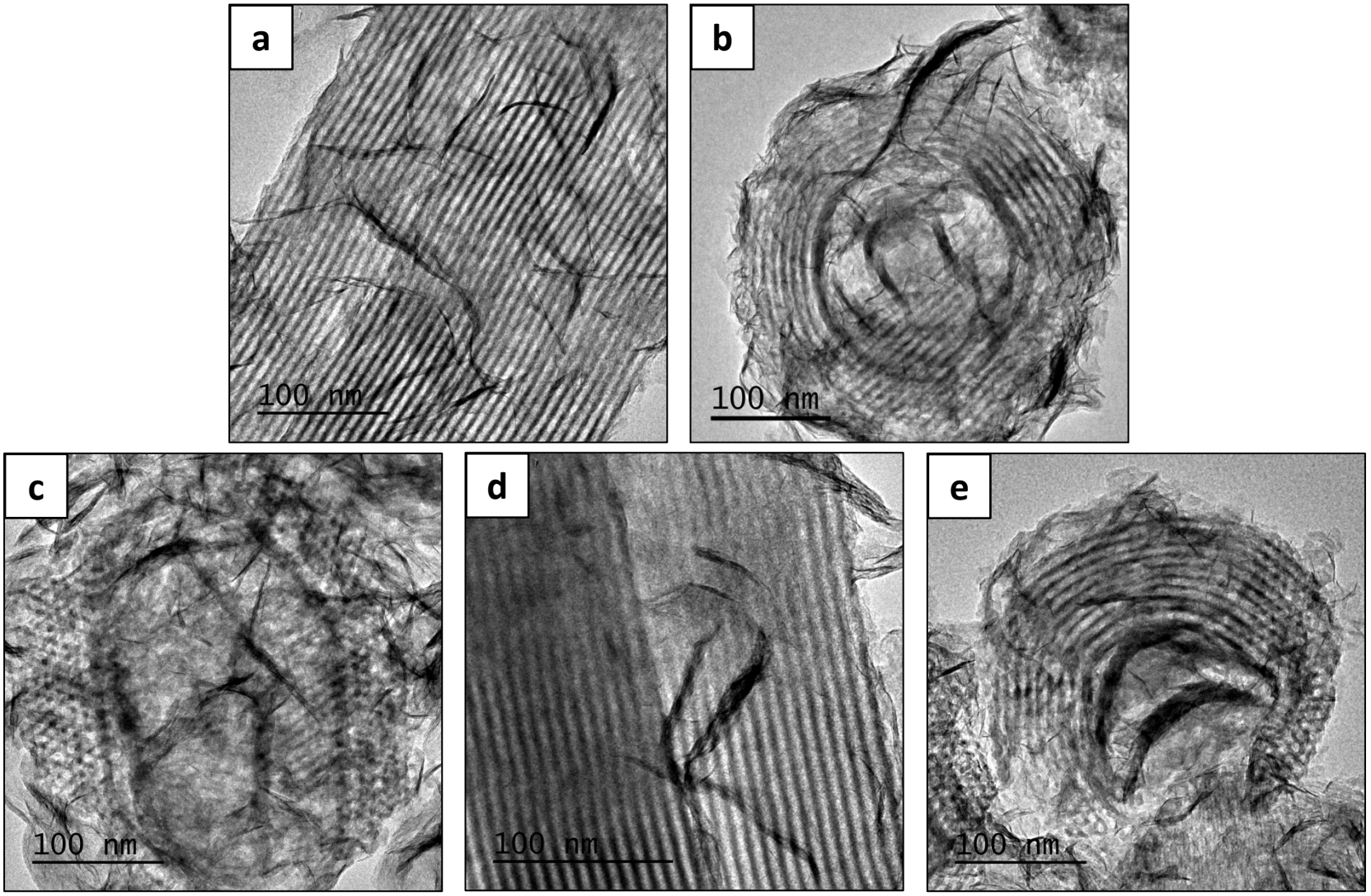

Figure 1. TEM images for calcined 10Ni/SBA-15 (a), 8Ni-2Co/SBA-15 (b), 5Ni-5Co/SBA-15 (c), 2Ni-8Co/SBA-15 (d) and 10Co/SBA-15 (e) catalysts.

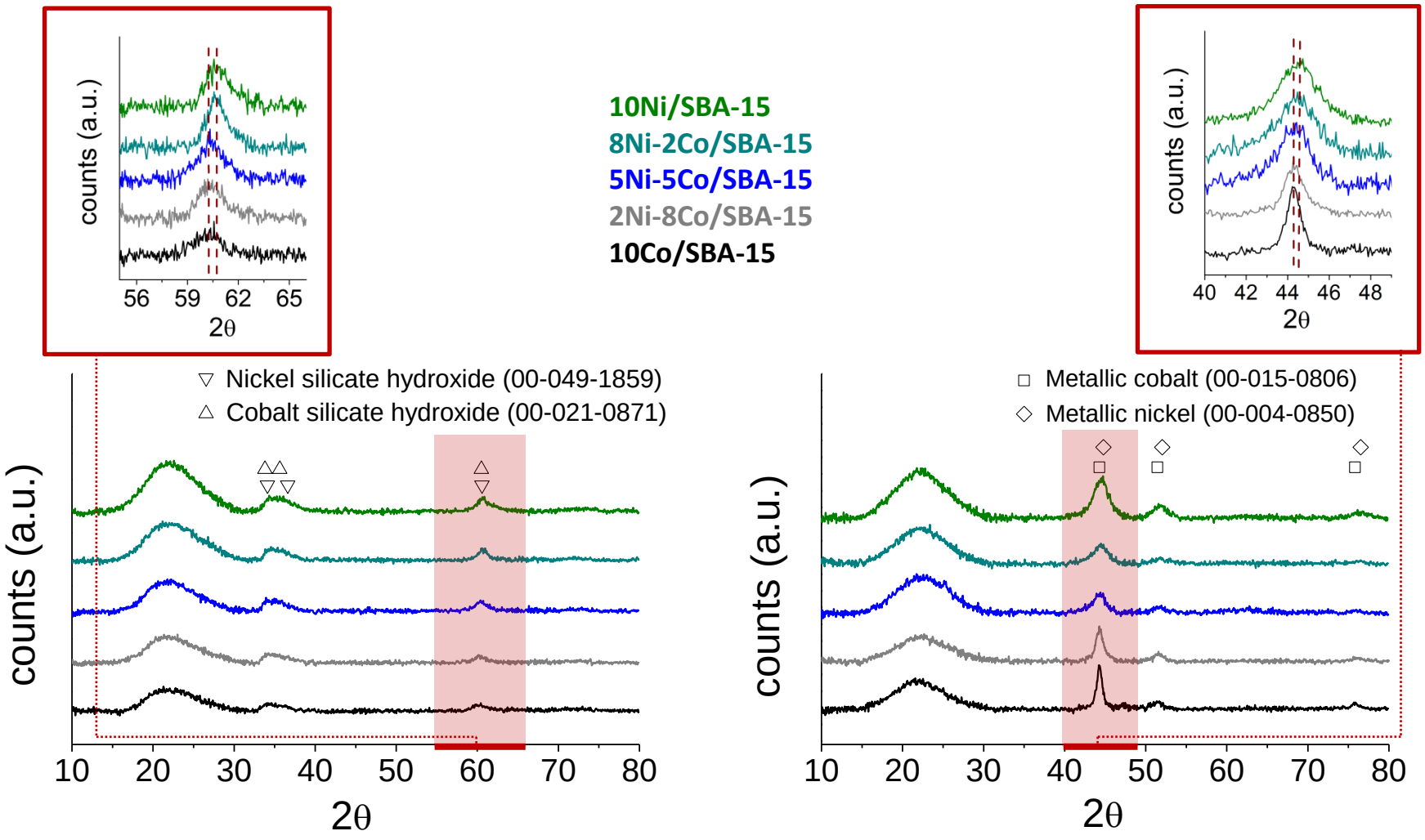

Figure 2. XRD patterns for (left) calcined and (right) treated in 5%H_2/Ar at 750 °C nickel-cobalt-based systems.

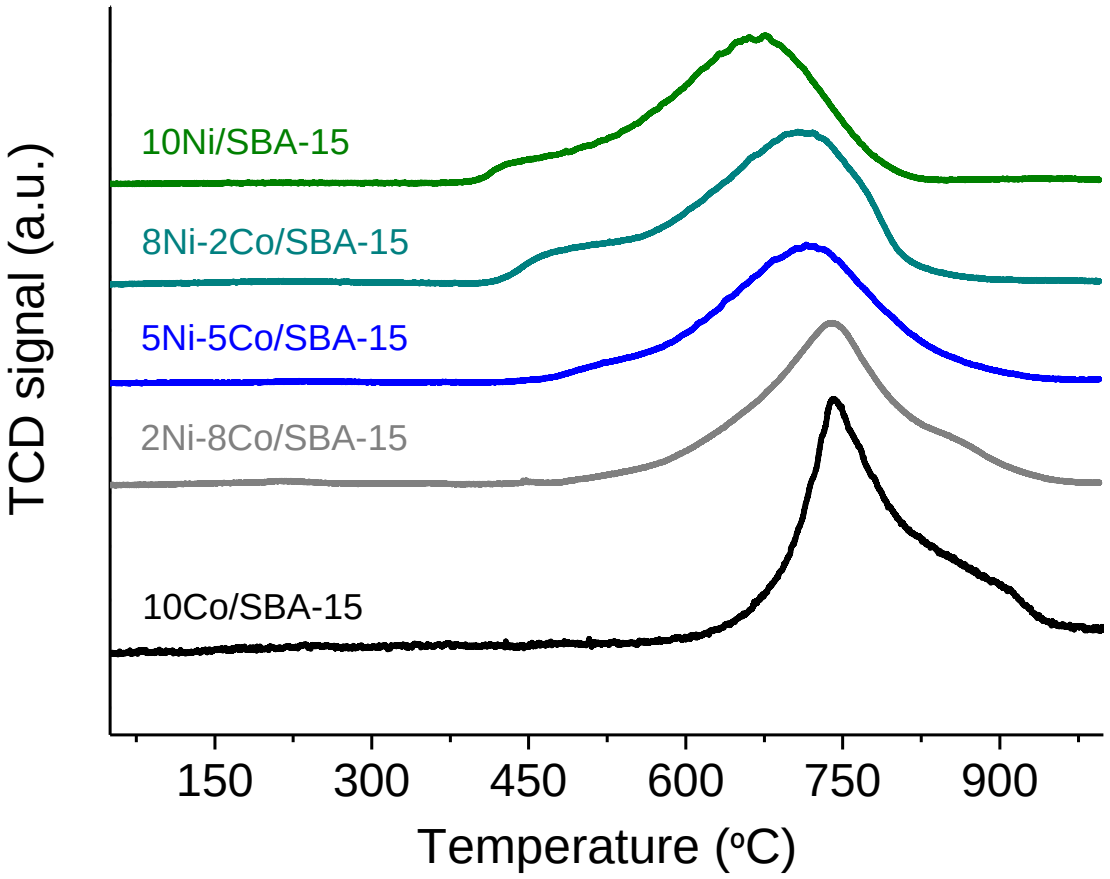

Figure 3. Temperature-programmed reduction profiles for the calcined Ni-Co/SBA-15 catalytic systems.

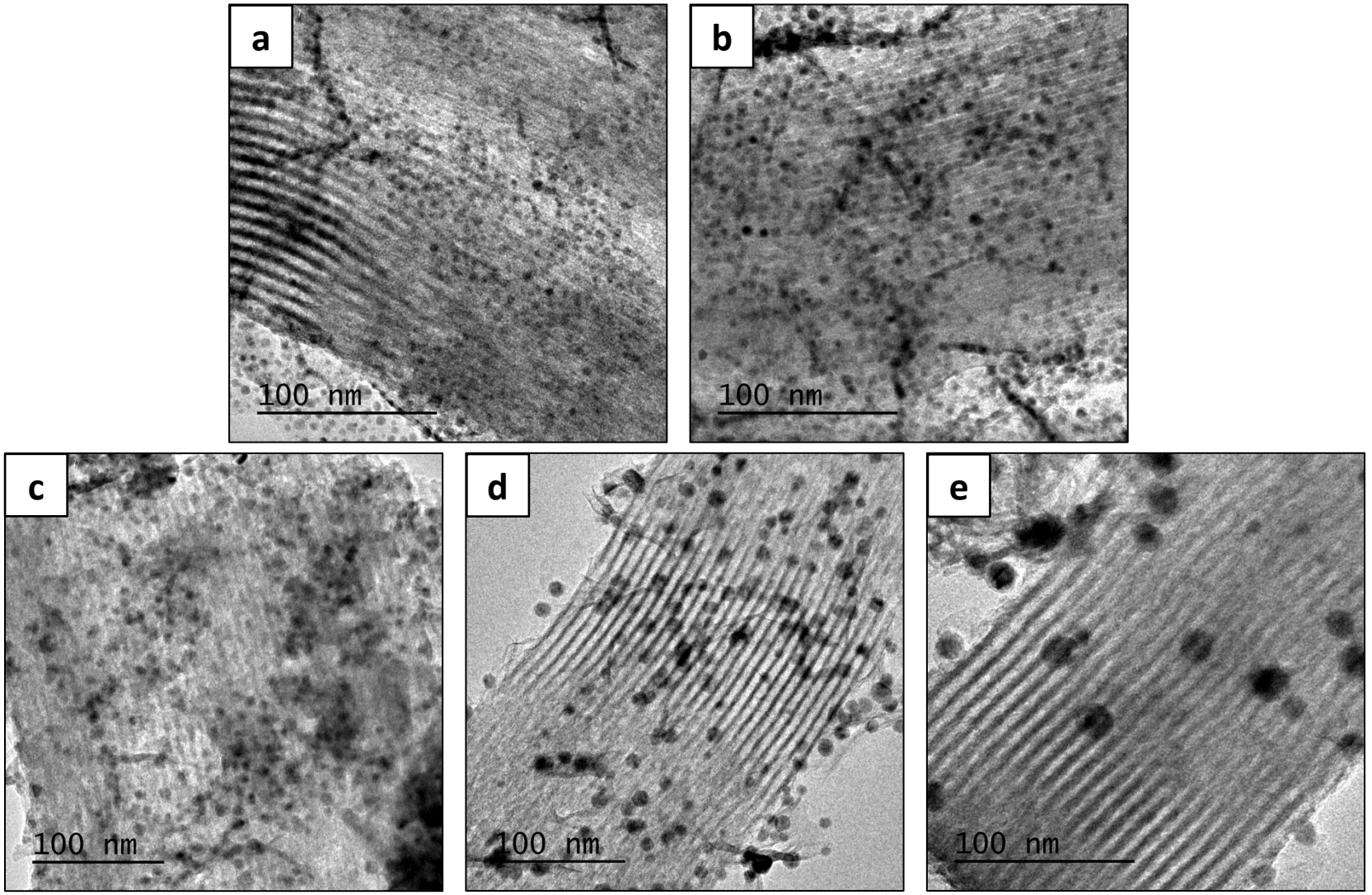

Figure 4. TEM images of 10Ni/SBA-15 (a), 8Ni-2Co/SBA-15 (b), 5Ni-5Co/SBA-15 (c), 2Ni-8Co/SBA-15 (d), and 10Co/SBA-15 (e), after hydrogen reduction at 750 °C.

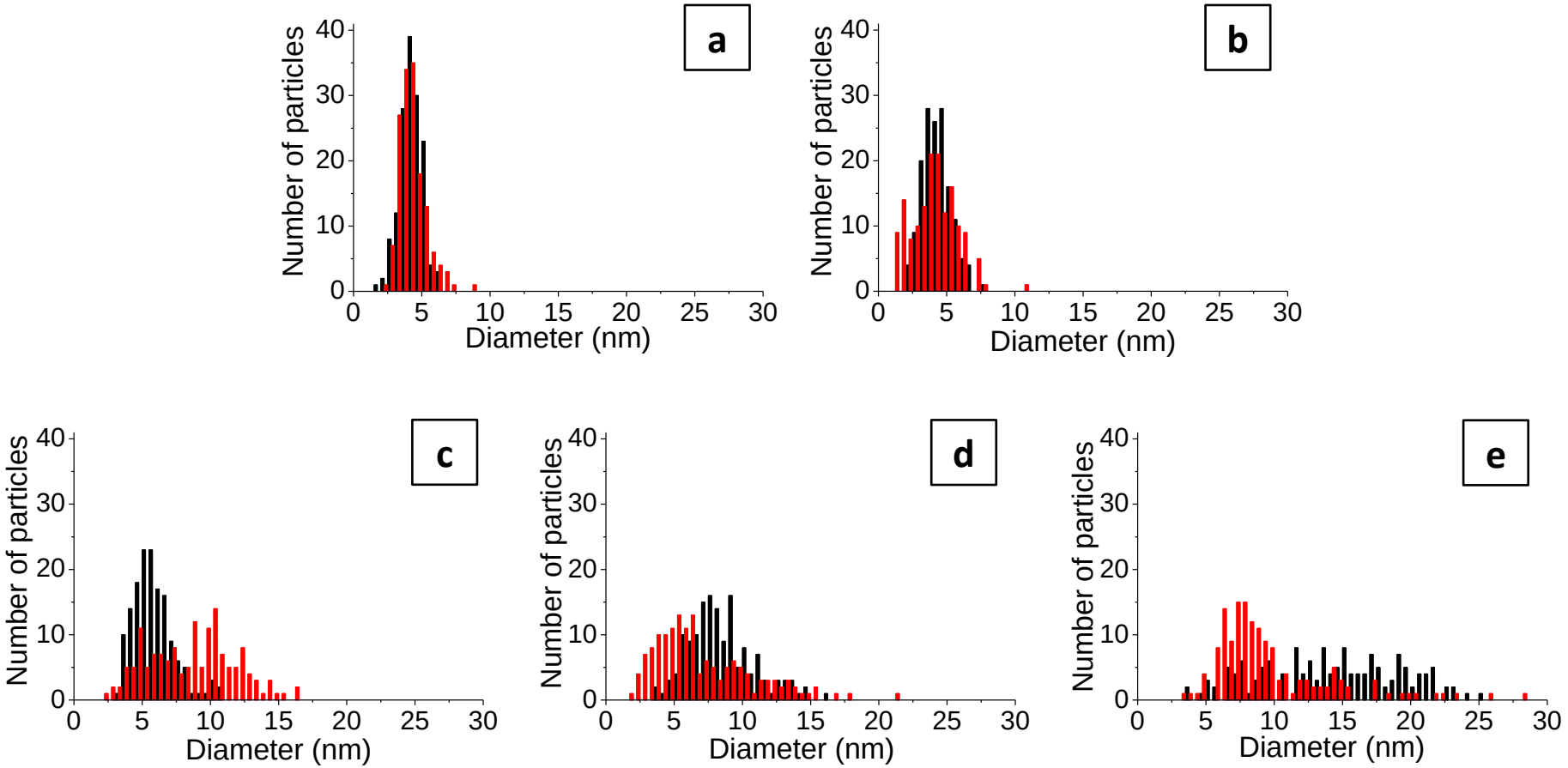

Figure 5. Histograms of particle sizes for 10Ni/SBA-15 (a), 8Ni-2Co/SBA-15 (b), 5Ni-5Co/SBA-15 (c), 2Ni-8Co/SBA-15 (d), and 10Co/SBA-15 (e), after reduction (black bars) and after being submitted to SRE reaction conditions (red bars).

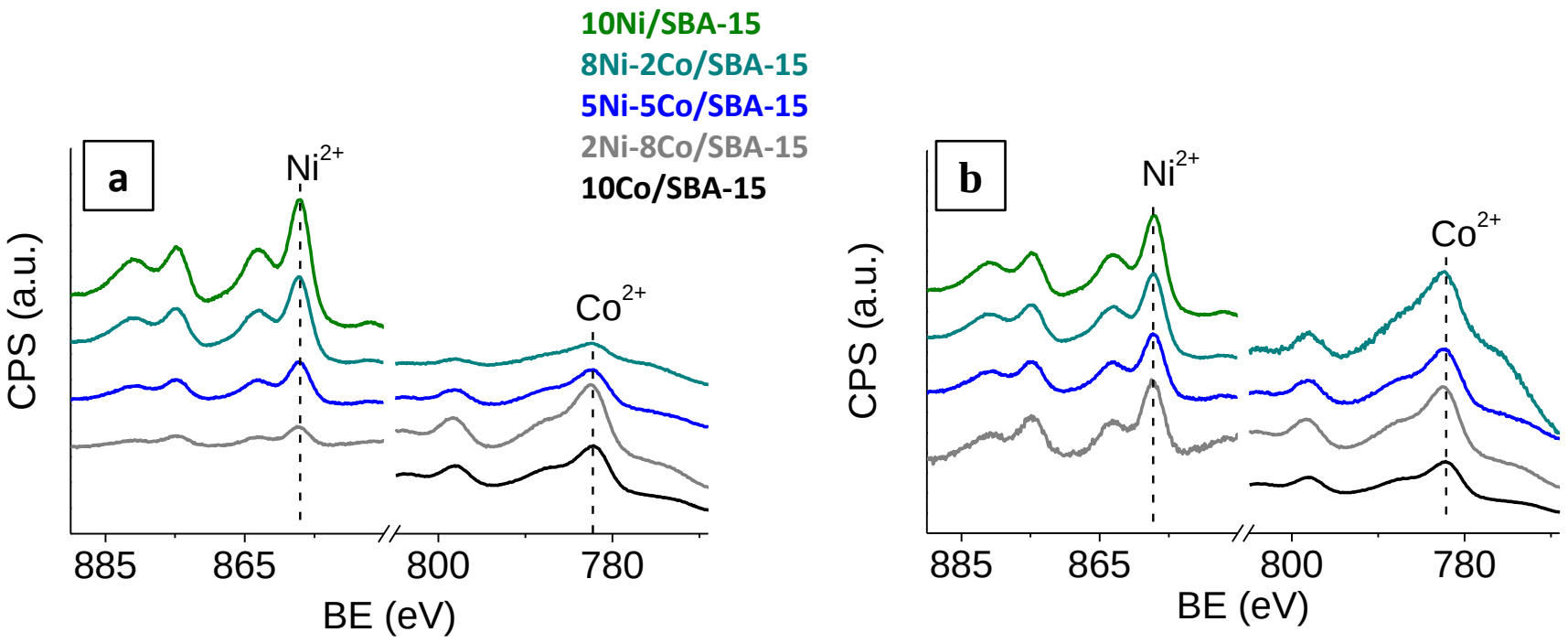

Figure 6. XPS spectra of calcined Ni-Co/SBA-15 systems (a) and same spectra normalized to metal percentage (b).

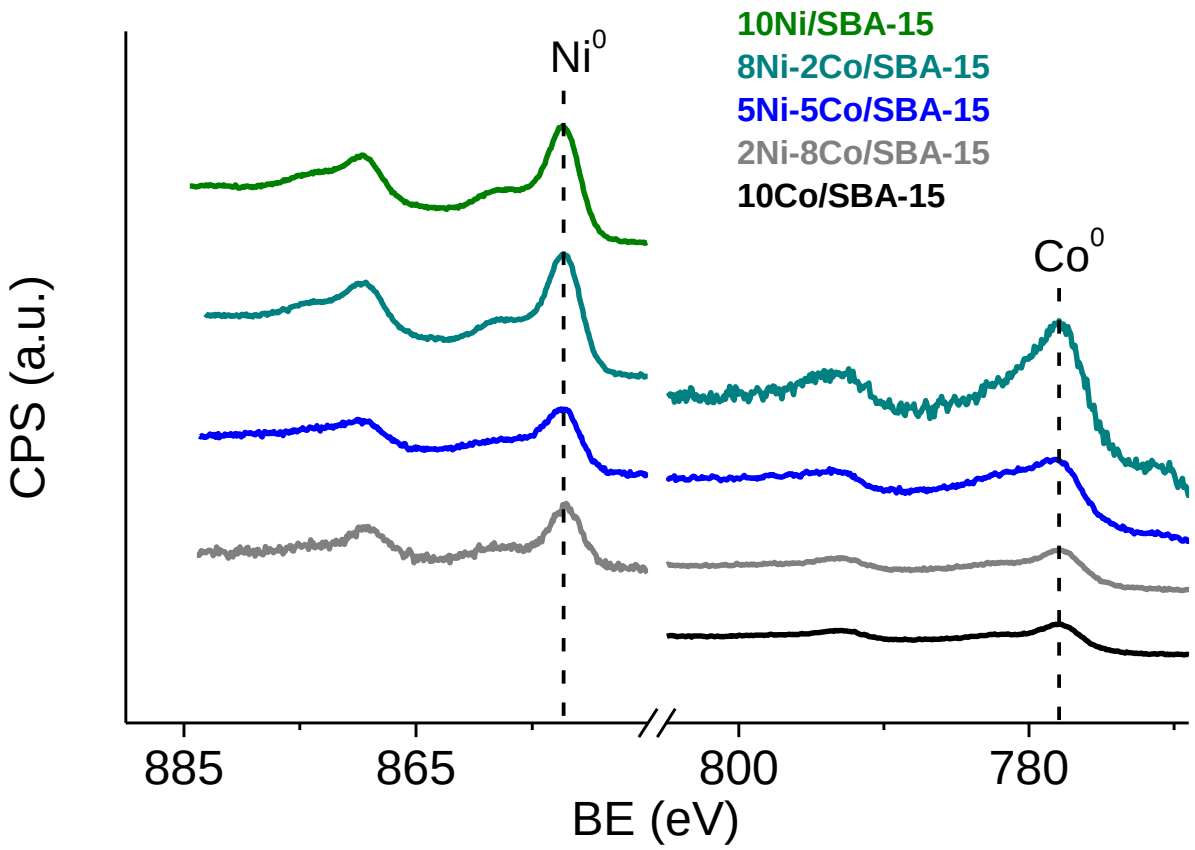

Figure 7. XPS spectra of reduced Ni-Co/SBA-15 systems normalized to metal percentage.

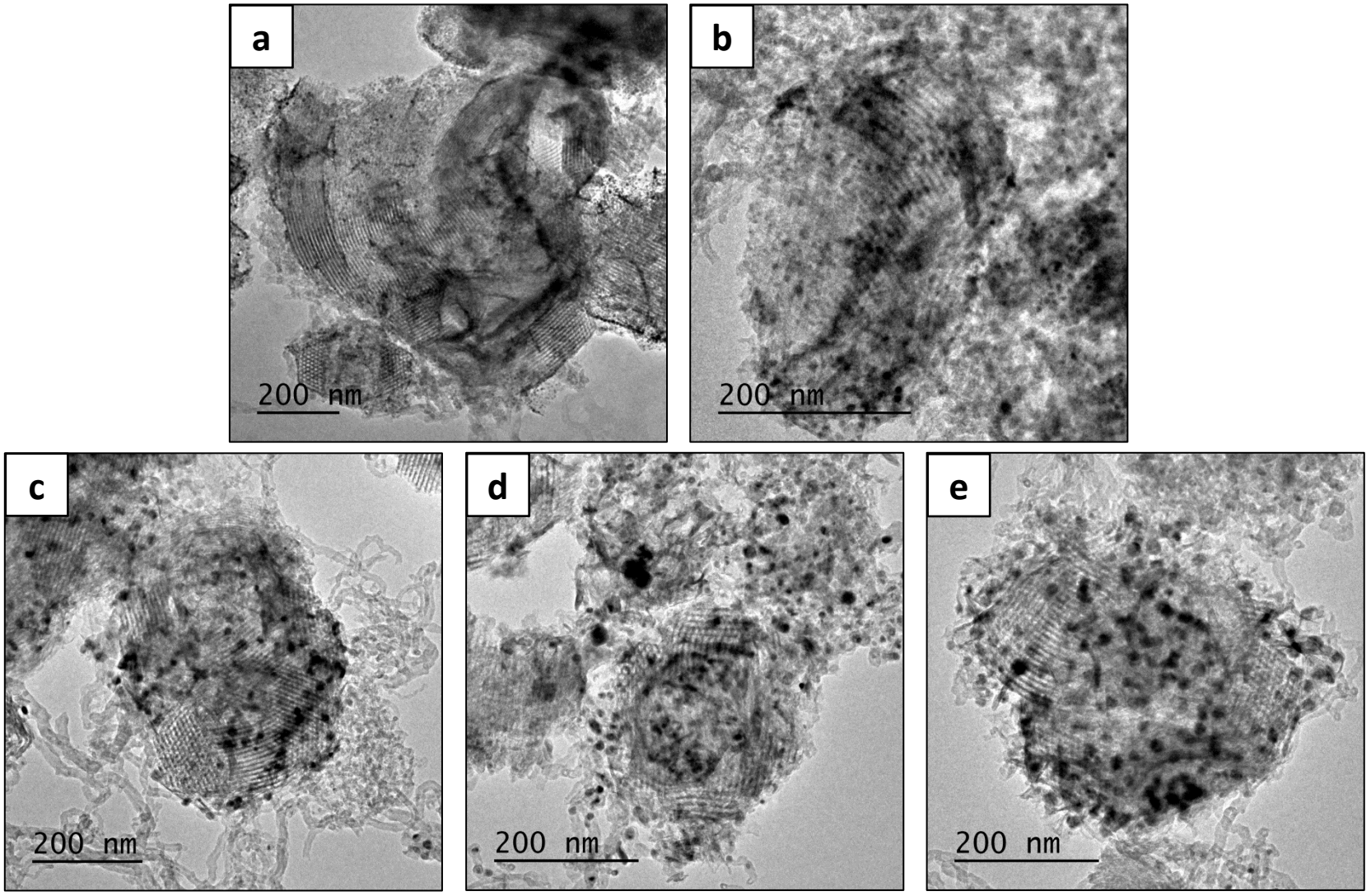

Figure 8. TEM images for 10Ni/SBA-15 (a), 8Ni-2Co/SBA-15 (b), 5Ni-5Co/SBA-15 (c), 2Ni-8Co/SBA-15 (d), and 10Co/SBA-15 (e), after SRE reaction.

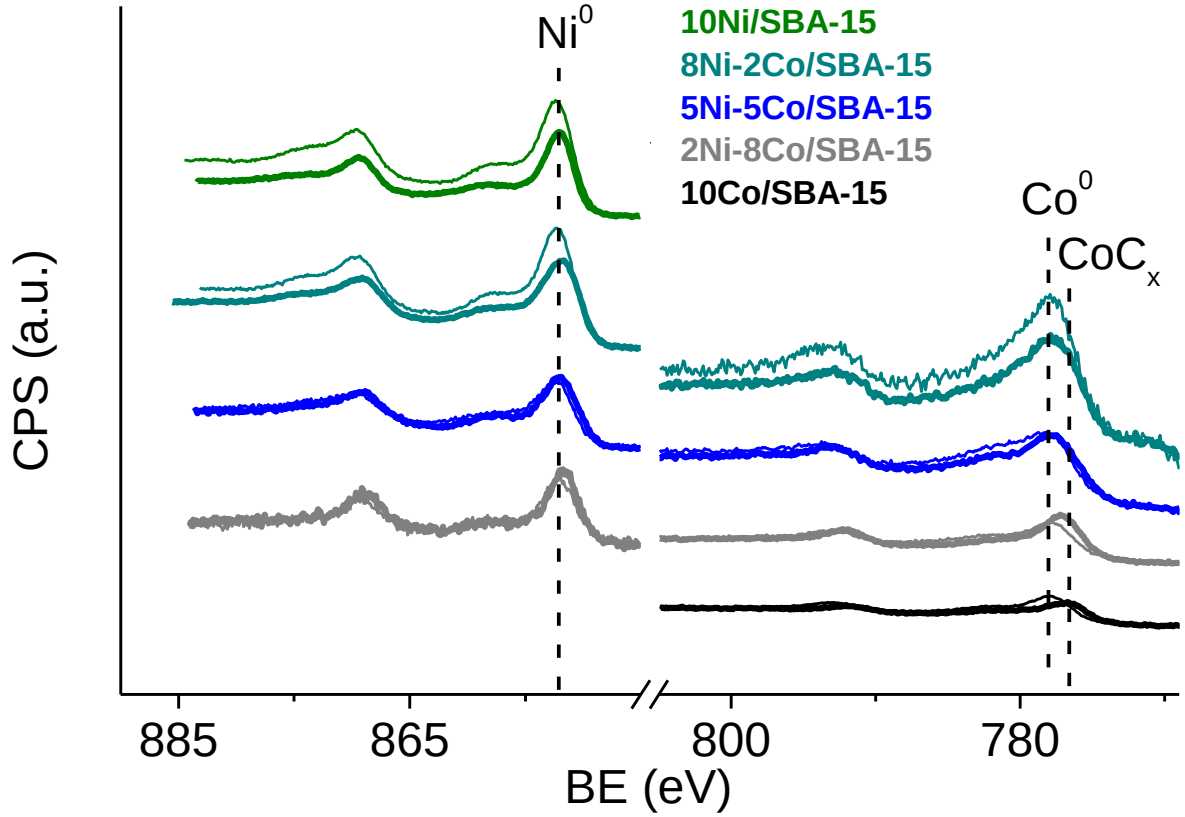

Figure 9. XPS spectra of reduced (thin line) and spent (thick line) Ni-Co/SBA-15 systems normalized to metal percentage.

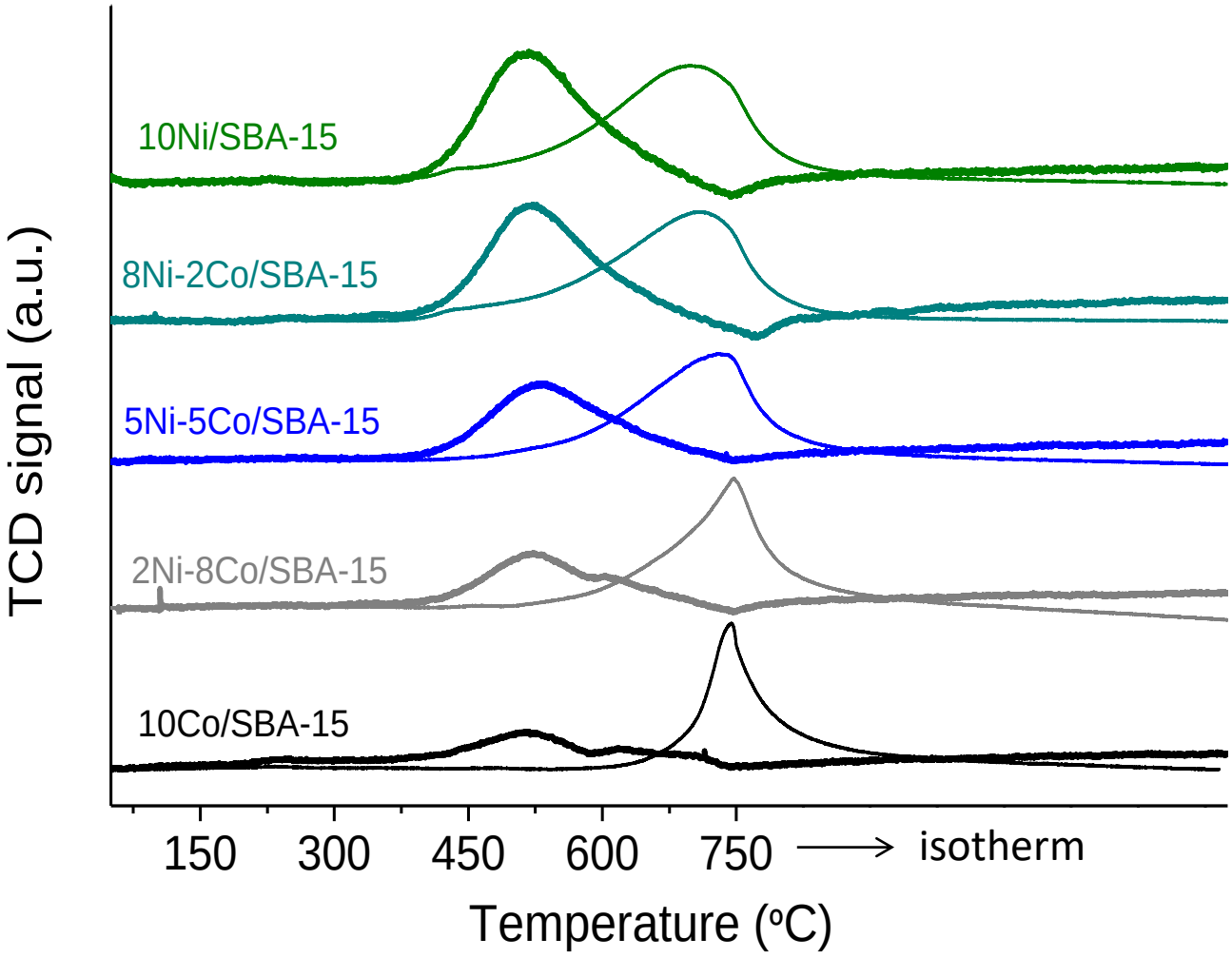

Figure 10. TPR profiles of Ni-Co/SBA-15 catalysts up to 750 °C plus 1h isotherm. Thin line: first TPR. Thick line: second TPR after SRE reaction.

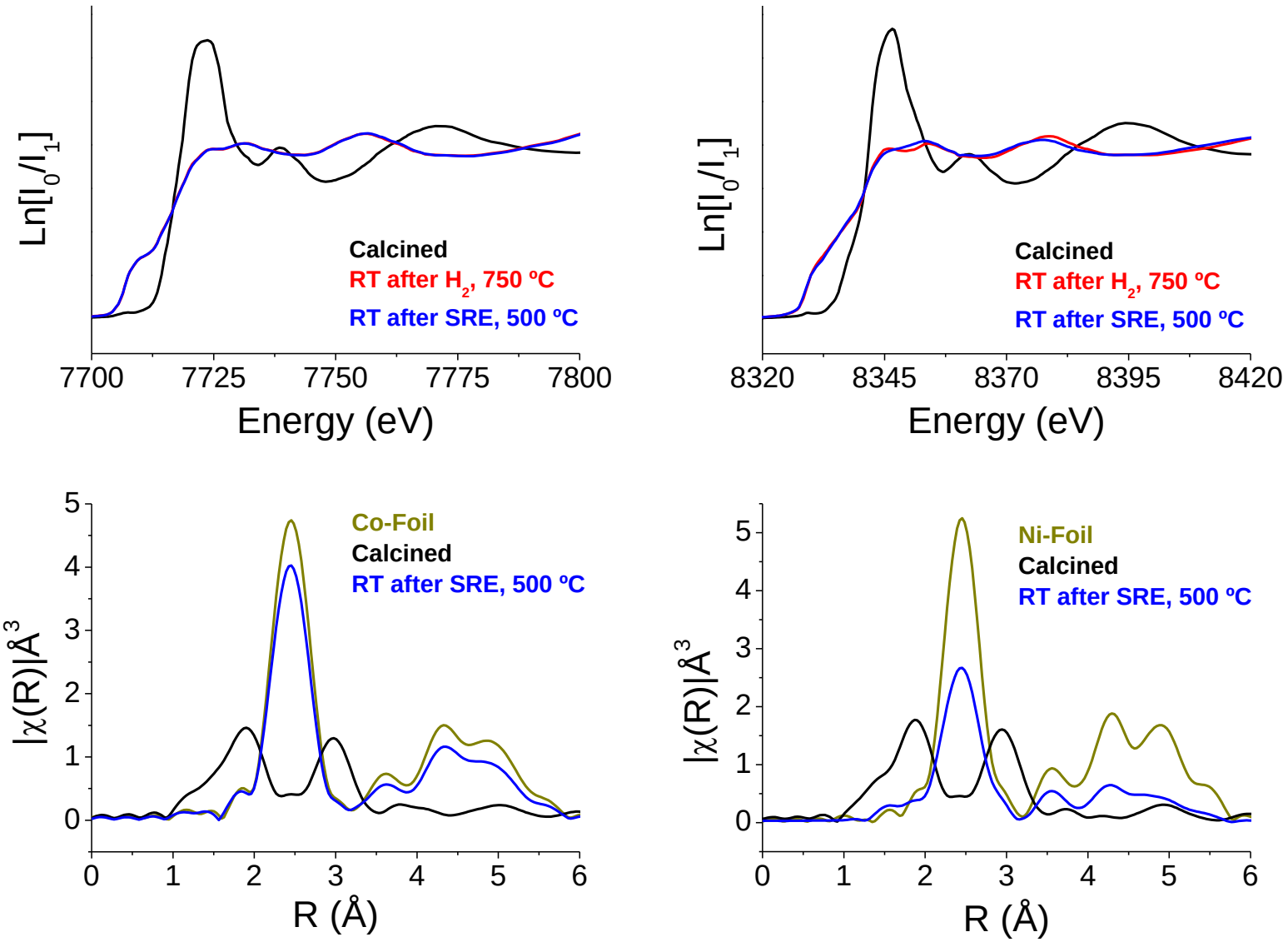

Figure 11. Co (left) and Ni (right) K-edge XANES spectra and Fourier transform functions of the EXAFS oscillations after different treatments.

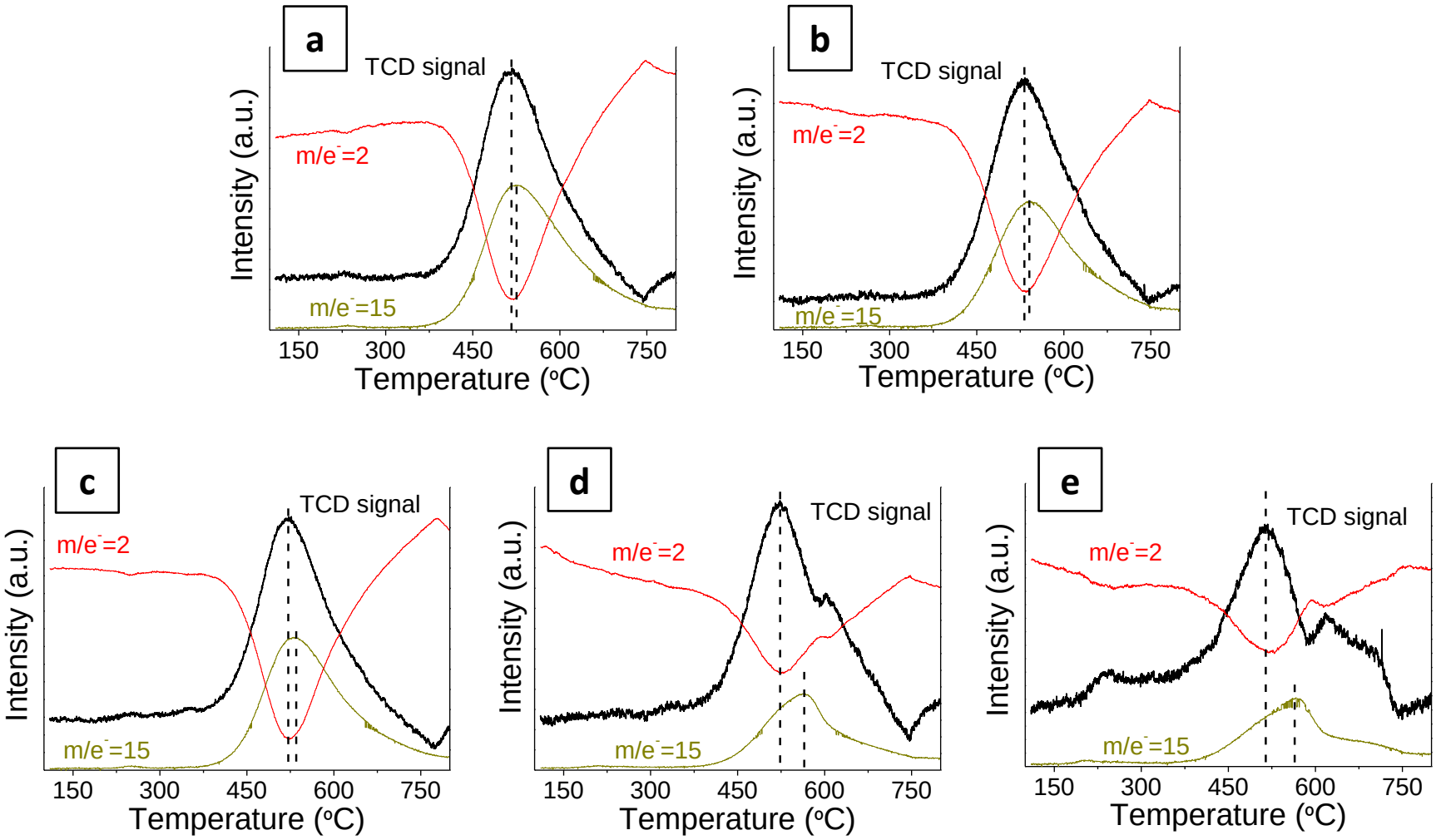

Figure 12. TCD and Mass Spectrometer signals coming from H_2 ($m/e^-=2$) and methane ($m/e^-=15$) for 10Ni/SBA-15 (a), 8Ni-2Co/SBA-15 (b), 5Ni-5Co/SBA-15 (c), 2Ni-8Co/SBA-15 (d), and 10Co/SBA-15 (e).

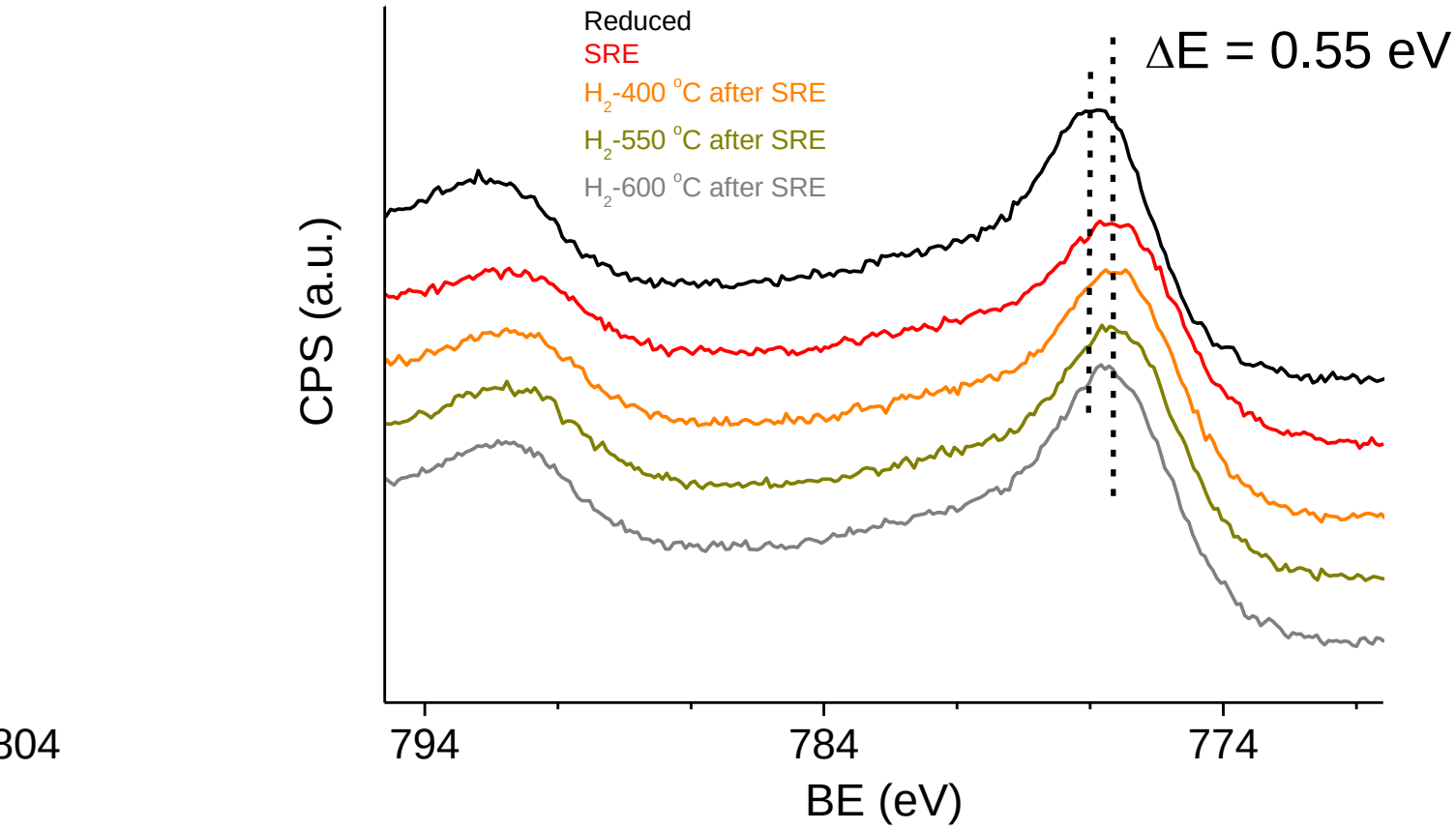

Figure 13. XPS spectra of reduced, spent and hydrogenated 10Co/SBA-15 system.